The Astrophysical Journal, 979:236 (11pp), 2025 February 1 https://doi.org/10.3847/1538-4357/ada26f

The Coronal Power Spectrum from MHD Mode Conversion above Sunspots

Hemanthi Miriyala[1], Richard J. Morton[1], Elena Khomenko[2,3], Patrick Antolin[1], and Gert J.J. Botha[1]
[1] Department of Mathematics, Physics and Electrical Engineering, Northumbria University, Newcastle upon Tyne, NE1 8ST, UK; hemanthi.miriyala@northumbria.ac.uk
[2] Instituto de Astrofísica de Canarias, 38205, La Laguna, Tenerife, Spain
[3] Departamento de Astrofísica, Universidad de La Laguna, 38205, La Laguna, Tenerife, Spain
Received 2024 October 16; revised 2024 December 13; accepted 2024 December 20; published 2025 January 29

Abstract

Sunspots are intense regions of magnetic flux that are rooted deep below the photosphere. It is well established that sunspots host magnetohydrodynamic waves, with numerous observations showing a connection to the internal acoustic (or *p*-)modes of the Sun. The *p*-modes are fast waves below the equipartition layer and are thought to undergo a double mode conversion as they propagate upward into the atmosphere of sunspots, which can generate Alfvénic modes in the upper atmosphere. We employ 2.5D magnetohydrodynamic numerical simulations to investigate the adiabatic wave propagation and examine the resulting power spectra of coronal Alfvénic waves. A broadband wave source is used, which has a 1D power spectrum mimicking aspects of the observed *p*-mode power spectrum. We examine magnetoacoustic wave propagation and mode conversion from the photosphere to the corona. Frequency filtering of the upwardly propagating acoustic waves is a natural consequence of a gravitationally stratified atmosphere and plays a key role in shaping the power spectra of mode-converted waves. We demonstrate that the slow and fast magnetoacoustic waves and Alfvén waves above the equipartition layer have similarly shaped power spectra, which are modified versions of the driver spectrum. Notably, the results reveal that the coronal wave power spectra have a peak at a higher frequency than that of the underlying *p*-mode driver. This matches observations of coronal Alfvénic waves and further supports the role of the mode conversion process as a mechanism for Alfvénic wave generation in the Sun's atmosphere.

Unified Astronomy Thesaurus concepts: Magnetohydrodynamical simulations (1966); Solar coronal waves (1995); Alfvén waves (23); Sunspots (1653)

1. Introduction

Magnetohydrodynamic (MHD) waves are considered to play a key role in the transfer of energy through the Sun's atmosphere (D. E. Osterbrock 1961; D. B. Jess et al. 2015; V. M. Nakariakov & D. Y. Kolotkov 2020; T. Van Doorsselaere et al. 2020), carrying energy from the convective motions in the photosphere out into the corona and beyond. In an inhomogeneous plasma, such as the Sun's atmosphere, a variety of MHD wave modes can exist beyond the traditional slow, fast, and Alfvén modes (H. C. Spruit 1982; P. M. Edwin & B. Roberts 1983). Inhomogeneity perpendicular to the magnetic field leads to MHD waves having mixed properties (M. L. Goossens 2019). As such, a variety of modes can be considered Alfvénic in nature (M. Goossens et al. 2009). Their characteristic incompressibility indicates that the Alfvénic waves play a crucial role in transporting energy through the solar atmosphere (e.g., R. J. Morton et al. 2023).

Alfvénic modes are generally considered to be driven by the buffeting of magnetic fields in the photosphere (e.g., S. R. Cranmer & A. A. van Ballegooijen 2005). However, global observations of coronal Doppler velocities suggest Alfvénic waves have an enhanced power around 4 mHz (R. Morton et al. 2019), which is not expected from convective driving. It has been suggested that the enhanced power can be linked with the peak of the *p*-mode power spectrum in the photosphere, which lies at ~3 mHz (e.g., S. C. Hansen & P. S. Cally 2012). The close proximity of the peaks in frequency space has been taken as evidence that the coronal Alfvénic waves are somehow influenced by the *p*-modes.

Previous studies have demonstrated the possibility of converting acoustic modes to Alfvén waves (via conversion to and from the fast magnetoacoustic mode; e.g., P. S. Cally & M. Goossens 2008; T. Felipe 2012; E. Khomenko & P. S. Cally 2012). A number of other studies have also implemented a broadband *p*-mode driver in order to excite coronal Alfvénic waves. For instance, H. Kuniyoshi et al. (2024) used 2D simulations to demonstrate high-frequency transverse spicule oscillations driven by *p*-modes, although the underlying mechanism exciting these oscillations remains unclear. Y. Gao et al. (2023) utilized a 3D model of a closed magnetic loop and excite waves with a monoperiodic *p*-mode driver. There is certainly the possibility of linear mode conversion in such simulations, but their focus is on the generation of standing waves. S. J. Skirvin et al. (2023) investigated the mechanism for exciting transverse Alfvénic waves using an inclined *p*-mode wave driver, which breaks symmetry and utilizes pressure to displace the magnetic field. However, this study did not explicitly address mode conversion. Related work by S. J. Skirvin & T. Van Doorsselaere (2024) has explored the role of transverse structuring in mode conversion within the lower solar atmosphere. Despite such studies, it has not yet been demonstrated that enhancements in coronal power spectra can arise from the *p*-mode excitation of Alfvénic waves.

The *p*-modes are the pressure perturbations trapped below the photosphere (T. Sakurai 2017) and are absorbed by regions of high magnetic fields, such as sunspots or magnetic bright points associated with the network regions in the quiet Sun.

Due to the abundant magnetic field, the p-modes are funnelled as magnetoacoustic waves into the solar atmosphere (H. C. Spruit et al. 1992; P. S. Cally & T. J. Bogdan 1997). The p-modes are predominantly acoustic in nature and are subject to the acoustic cutoff frequency. The frequency of the cutoff arising in a gravitationally stratified plasma is (from a WKB approximation) given by

$$\nu_{\rm ac} = \frac{\gamma g}{4\pi c_s}, \quad (1)$$

where c_s is the sound speed, γ is the ratio of specific heats, and g is gravity (V. Landgraf 1997; A. Jiménez et al. 2011; E. Khomenko & P. Cally 2012). Acoustic (fast) modes in a high-beta plasma (i.e., in the low photosphere and solar interior) propagate isotropically, hence are little influenced by the magnetic field, although when the Alfvén speed, $v_{\rm A}$, and sound speed are comparable ($c_s \approx v_{\rm A}$), the magnetic field can influence wave propagation (P. S. Cally 2006).

In a low-beta plasma ($c_s < v_{\rm A}$), the acoustic waves are the slow modes and are field-guided. Hence, the cutoff frequency is modified by effective gravity along the inclined flux tubes, as the slow magnetoacoustic waves have a preferred path of propagation dictated by the inclined magnetic field (e.g., H. Schunker & P. S. Cally 2006). The effective cutoff is

$$\nu_{\rm ac,eff} = \nu_{\rm ac} \cos\theta,$$

where the cosine of the inclination angle, θ, is defined with respect to the local vertical. The influence of the effective acoustic cutoff on the slow modes is thought to be the basis of the well-known phenomena associated with sunspot oscillations. One is that sunspots' umbrae show power spectra dominated by oscillations with frequencies of ~3 mHz in the photosphere but dominated by ~5 mHz oscillations in the chromosphere (see, e.g., T. J. Bogdan & P. G. Judge 2006; R. Centeno et al. 2006; T. Felipe et al. 2010). Moreover, the variation of the peak oscillatory power with inclination has also been reported in observations of sunspots' penumbral chromospheres. The frequency of slow magnetoacoustic waves with the largest power decreases with distance from the spot center (D. Jess et al. 2013; D. B. Jess & G. Verth 2016; R. J. Morton et al. 2021).

P. S. Cally & M. Goossens (2008) first discussed mode conversion as a mechanism for producing Alfvén waves from p-modes. They demonstrated that Alfvén waves can be generated by the mode conversion of fast magnetoacoustic waves when the magnetic field is inclined with respect to the plane of wave propagation. Motivated by these studies, E. Khomenko & P. Cally (2012) and E. Khomenko & P. S. Cally (2012) employed 2.5D numerical simulations in sunspot-like regions to understand the efficiency of the conversion from p-modes to Alfvén waves. The p-modes are fast acoustic waves below the equipartition layer (the layer where $c_s = v_{\rm A}$). The fast acoustic waves largely enter the low-beta atmosphere as fast magnetic waves, with mode conversion changing their character from acoustic to magnetic. However, around the equipartition layer, the fast acoustic waves can also be transmitted as slow magnetoacoustic modes for a narrow range of magnetic field inclinations (e.g., P. S. Cally 2006; H. Schunker & P. S. Cally 2006).

The fast magnetoacoustic waves then undergo significant reflection due to the rapidly increasing Alfvén speed in the upper atmosphere at the locations where their horizontal phase speed matches the local Alfvén speed i.e., $\omega/k_h = v_{\rm A}$, where ω is the angular frequency and k_h is the horizontal wavenumber (P. S. Cally & S. C. Hansen 2011). The fast-to-Alfvén conversion coefficient is then predominantly based on the horizontal wavenumber (k_h), magnetic field inclination (θ) from the stratification direction, and the azimuthal angle (ϕ) of the wavevector with respect to the plane containing the stratification and magnetic field directions (P. S. Cally & S. C. Hansen 2011). Hence, there is effectively a double mode conversion in getting from acoustic to Alfvén waves. The extent of the acoustic-to-Alfvén conversion is largely influenced by the magnetic field inclination and azimuth angles around the equipartition layer (P. S. Cally & M. Goossens 2008; E. Khomenko & P. S. Cally 2012). P. S. Cally & M. Goossens (2008) reported that magnetic field inclinations between 30° and 40° and azimuth angles between 60° and 80° at the equipartition layer favor the double mode conversion, and the resultant Alfvén fluxes are significantly higher than the acoustic fluxes.

Given the nature of MHD wave propagation in the lower solar atmosphere, how then might the observed enhancement of coronal Alfvénic wave power occur? And why is the peak at a frequency of 4 mHz while the p-modes peak around 3.3 mHz? We suggest the shape of the coronal Alfvénic power spectrum could be defined by the atmospheric filtering of the p-mode power spectrum. The acoustic cutoff frequency is able to modify the acoustic power spectrum through a frequency filtering of the upwardly propagating acoustic modes.

If we consider the acoustic spectrum at the equipartition layer, the effect of the cutoff will be to skew the peak of the power to higher frequencies than those of the p-mode spectrum, as the lower frequencies are truncated. The mode conversions from fast (acoustic) to fast (magnetic) and from fast (magnetic) to Alfvén are linear; hence, there is no change in wave frequency. As such, one should also expect the power spectra of fast and Alfvén modes, generated by mode conversion from upwardly propagating acoustic modes, to have a peak frequency higher than those of the p-modes. The frequency filtering will depend on the height of the equipartition layer. The cutoff frequency varies as a function of height in the solar atmosphere, having its largest value at the temperature minimum. If the equipartition layer occurs below the temperature minimum along a nearly vertical field line, as in a sunspot umbra, then the peak frequency of the fast- and Alfvén-mode spectra will likely be lower than that of the slow modes. This is because the slow mode is continuously influenced by the effect of the cutoff after propagating past the equipartition layer and there is further reflection due to the transition region.

In the following, we examine the role the acoustic cutoff on MHD wave propagation with numerical simulations. Previous work on the fast-to-Alfvén mode conversion focused efforts on understanding the fundamentals of the process, generally opting to use monochromatic wave drivers for clarity (E. Khomenko & P. Cally 2012; E. Khomenko & P. S. Cally 2012). A nonmonochromatic driver was used by T. Felipe et al. (2010), but their simulations did not reach the corona and the power spectra of the Alfvénic waves did not appear to be of interest. As such, there has not been an investigation into what aspects of the p-mode spectrum are imparted upon the coronal Alfvénic waves. Hence, the main objective of this work is to examine the nature of the coronal Alfvénic wave power

spectrum when the system is driven by a broadband driver that resembles the p-modes. We employ a modified version of the sunspot model used in the previous studies of E. Khomenko & P. Cally (2012) and E. Khomenko & P. S. Cally (2012), and we extend the atmosphere into the transition region and corona. Acoustic modes are driven with a broadband driver and we investigate the adiabatic wave propagation, examining the resulting power spectra of the coronal Alfvén waves.

2. Numerical Setup

2.1. Numerical Scheme

Following E. Khomenko & P. Cally (2012) and E. Khomenko & P. S. Cally (2012), we use the MANCHA code to solve the nonlinear equations for perturbations where the equilibrium state is removed from the equations (see E. Khomenko & M. Collados 2006, 2008; T. Felipe et al. 2010; M. Modestov et al. 2024 for more details on MANCHA). The system of MHD equations to be solved is written in conservative form, namely:

$$\frac{\partial \rho}{\partial t} + \nabla \cdot (\rho \boldsymbol{v}) = 0, \tag{2}$$

$$\frac{\partial (\rho \boldsymbol{v})}{\partial t} + \nabla \cdot \left[\rho \boldsymbol{v}\boldsymbol{v} + \left(p + \frac{\boldsymbol{B}^2}{2\mu_0} \right) \boldsymbol{I} - \frac{\boldsymbol{B}\boldsymbol{B}}{\mu_0} \right] = \rho \boldsymbol{g}, \tag{3}$$

$$\frac{\partial \boldsymbol{B}}{\partial t} = \nabla \times (\boldsymbol{v} \times \boldsymbol{B}), \tag{4}$$

where $\boldsymbol{I}$ is the identity tensor and E represents the total energy and is expressed as

$$E = \frac{1}{2}\rho v^2 + \frac{p}{\gamma - 1} + \frac{\boldsymbol{B}^2}{2\mu_0}. \tag{5}$$

Here, ρ is the density, v is the velocity, p is the gas pressure, B is the magnetic field, μ_0 is the magnetic permeability, and $\boldsymbol{g}$ is the gravitational acceleration. We also employ an ideal equation of state for which $\gamma = 5/3$. The MHD equations are solved with spatial and temporal discretizations that are centered, fourth-order-accurate, explicit finite-difference-scheme (A. Vögler et al. 2005), and fourth-order Runge–Kutta-scheme, respectively (E. Khomenko & M. Collados 2006; M. Modestov et al. 2024). Following E. Khomenko & P. S. Cally (2012), we use a 2.5D approximation to solve the equations, which allows for vectors in three spatial directions, but the derivatives are taken only in two directions (one vertical and one horizontal). Hence, the perturbations only propagate in the XZ-plane.

2.2. Magnetostatic Sunspot Model

To generate the background atmosphere upon which the wave propagation occurs, we choose to sample a 2D slice from a 3D atmosphere. For this purpose, we employ a sunspot model that closely resembles the one discussed in E. Khomenko & M. Collados (2008). The sunspot domain is a thick flux tube that is azimuthally symmetric with no twist. It is a current-distributed model that has the radial variations of field strength and gas pressure continuous across the spot, and it is constructed by merging a self-similar solution by B. Low (1980) in the deep layers with the model of V. J. Pizzo (1986) in the atmospheric layers. There is no sharp transition between the umbra and penumbra or between the penumbra and the field-free photosphere. The magnetic field inclination of the field lines changes gradually from the sunspot axis outward (see Figure 1). At the spot center, $(X, Y) = (0, 0)$ Mm, the magnetic field is 2200 G below the photosphere and gradually decreases with height. Readers are referred to E. Khomenko & M. Collados (2008) for details on the construction of the sunspot model.

There are a number of modifications to our model from that of E. Khomenko & M. Collados (2008). One adaption is that we elect to use the FAL-C model (J. M. Fontenla et al. 1993) as our quiet-Sun boundary (between 0.7 Mm and 2.2 Mm in height), which describes the upper photosphere and solar chromosphere (FAL-C is more consistent with the observed hydrogen and helium spectra than VAL-C; J. M. Fontenla et al. 1993).

In order to include a corona in the simulation domain, we choose to extend the atmosphere to 8 Mm above the photosphere. The upper 2 Mm of the domain are reserved for accommodating the boundary conditions at the top of the simulation domain. To extend the atmosphere of the quiet Sun, we first interpolate the temperature profile, using a polynomial function that begins at 2.2 Mm and attains a constant temperature by 5.5 Mm. We extend the atmosphere of the spot center likewise. Next, we calculate the pressure and density assuming hydrostatic equilibrium, as described in I. Santamaria et al. (2015). First, the pressure scale height is calculated as

$$H_p = \frac{R_{\rm gas} T}{g \mu_{\rm var}}, \tag{6}$$

which is used in the solution for the following hydrostatic equilibrium for pressure:

$$\frac{dp(z)}{dz} + \frac{p}{H_p} = 0. \tag{7}$$

Finally, we recover the density distribution from Equations (6) and (7) using

$$\rho = \frac{p}{g H_p}. \tag{8}$$

Here, p is the pressure, ρ is the density, $R_{\rm gas}$ is the gas constant, T is the temperature, and z is the height. We expect a varying degree of ionization of plasma with height. The mean atomic weight ($\mu_{\rm var}$) is approximately 0.5 in a single-fluid hydrogen-only plasma. Hence, the value of $\mu_{\rm var}$ is smoothly decreased until it reaches 0.5 in the corona for both the spot center and quiet Sun. We achieve this extrapolation past 2.2 Mm using an exponential function:

$$\mu_{\rm var} = 0.5 + e^{\kappa (z_i - z)}, \tag{9}$$

where κ is a scaling factor (sometimes referred to as a "steepness parameter"), and z_i is the initial height at which we begin the extrapolation. Hence, we extrapolate 1D atmospheric profiles past 2.2 Mm for both the quiet Sun and spot center, respectively. Once these models are established, a smooth transition between them for the gas-pressure and scale-height distributions is achieved and the force-balance equation along the magnetic field lines is iterated until a convergence criterion is reached (V. J. Pizzo 1986; E. Khomenko & M. Collados 2008).

Figure 1 displays the atmosphere at the center of the sunspot ($Y = 0$), cropped from -2 Mm to 5 Mm in the Z-direction and from 0 Mm to 38 Mm in the radial direction, for visualization purposes. Figure 1 clearly shows the variations across the

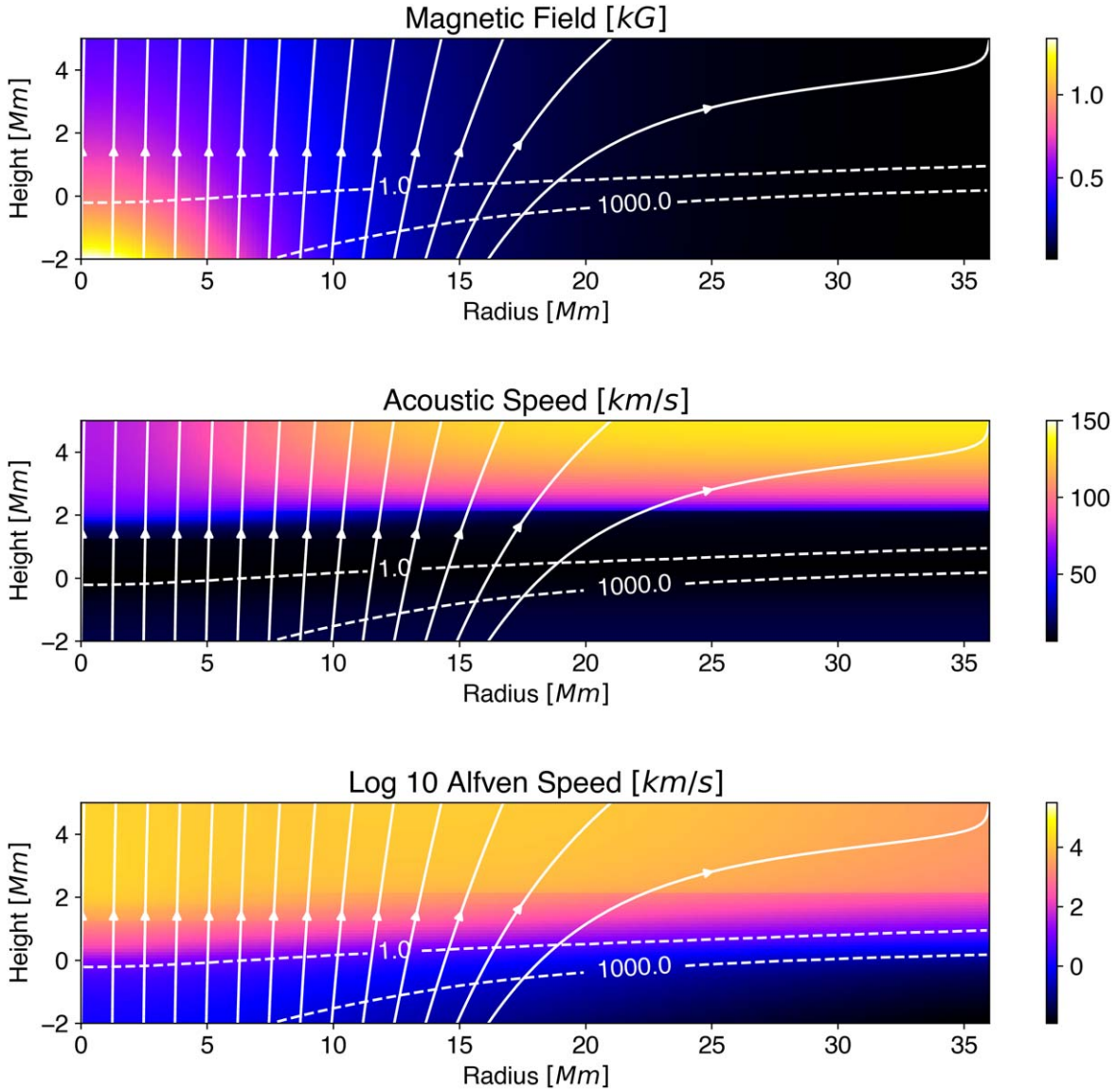

Figure 1. Topology of the expanded sunspot solution that includes the transition region and corona. Following E. Khomenko & M. Collados (2008), their Equations (6) and (7), the model is constructed using the following parameters: $a = 2h$, $h = 3$ Mm, $B_0 = 20000$ G, $z_0 = 1$ Mm, and $\eta = 3.5$. The white lines are magnetic field lines. The dashed lines with labels are the contours of the ratio of the sound speed and the Alfvén speed squared, (c_s^2/v_A^2).

domain in both the vertical and radial directions. The umbral and penumbral regions in the model can be differentiated based on the inclinations of the magnetic field lines.

For our 2.5D simulation, we use a vertical slice (*XZ*-plane) located at a distance of 7 Mm away from the center of the sunspot in the *Y*-direction. The domain is also restricted to 14.2 Mm in the *X*-direction (and is 10 Mm in the *Z*-direction). The magnetic structure of the magnetostatic solution is shown in the bottom left panel of Figure 2, which is a plot of the magnetic field strength with in-plane projections of the background magnetic field lines for the sunspot on an extended vertical scale of 10 Mm (i.e., [−2, 8] Mm). The temperature of the background atmosphere is shown in the top left panel of Figure 2. Examples of the 1D plasma profiles from the model can be observed in the right panels of Figure 2, located at $(X, Y) = (0, 7)$ Mm (the location is indicated by the vertical dashed line in the left panels of Figure 2). The spatial resolution across the domain is uniform and is set to 50 km in the horizontal *X*-direction and 20 km in the vertical *Z*-direction.

2.3. Diffusion Profile and Boundary Conditions

For the model boundary conditions in the horizontal direction, we follow C. D. MacBride et al. (2022). We use periodic boundary conditions on either side of our simulation domain, by reflecting the model horizontally and then shifting the model by half the original width, such that the original domain remains in the center of the *X*-axis. The numerical domain is large enough such that we do not see the wave entering back from the outer edges. Despite having our driver exciting perturbations with small amplitudes, they undergo appreciable amplification with height due to stratification. In order to reduce the reflections from the top boundary layer, we introduce a layer of diffusion on the top boundary above 4 Mm to 8 Mm. The diffusion profile is constructed using a sigmoid function, given by

$$D = 1/(1 + e^{\kappa(z - z_c)}). \quad (10)$$

Here, κ is a scaling factor, z is the height, and z_c is the height at which the sigmoid is centered. From Figure 3, it can be seen

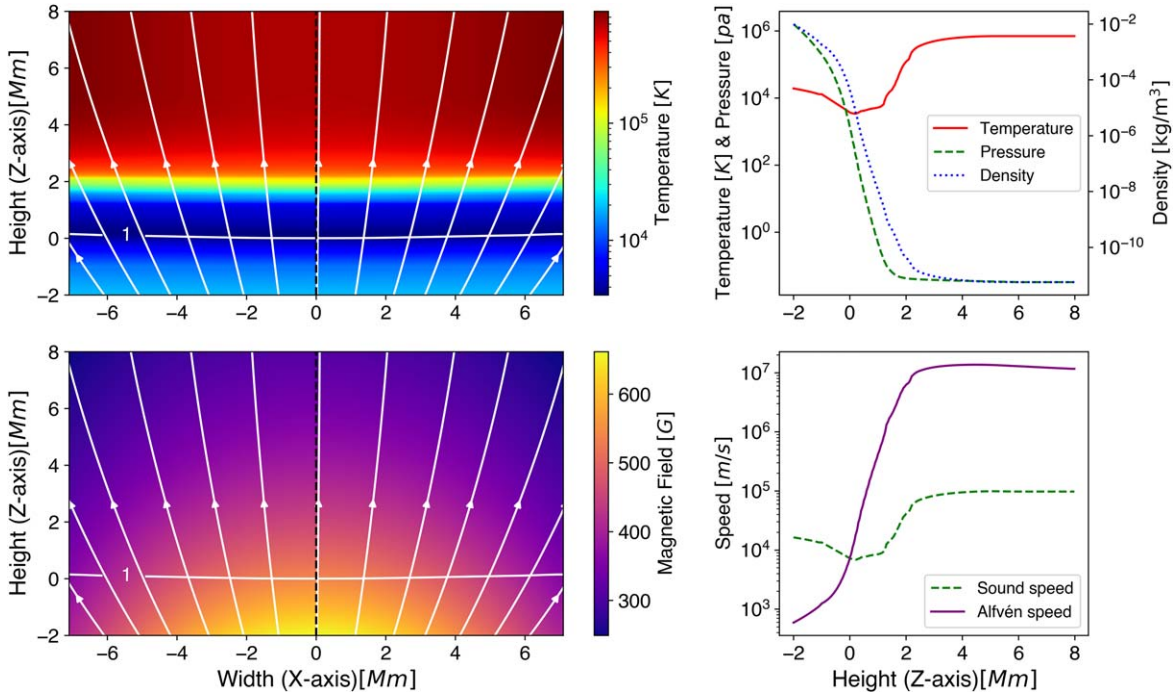

Figure 2. Background atmosphere taken at $Y = 7$ Mm (from the Y-origin at the spot center). The top and bottom left panels show the temperature and magnetic field variations of the background atmospheric conditions, respectively. The white contours with arrows show the in-plane projections of the background magnetic field lines, and the near-horizontal curve across the domain is the equipartition layer where $c_s/v_A = 1$. The top right panel shows the plasma properties as a function of height at the center of the domain (corresponding to the vertical dashed line in the left panels). Similarly, the bottom right panel shows the variation of sound and Alfvén speeds as a function of height at the center of the domain.

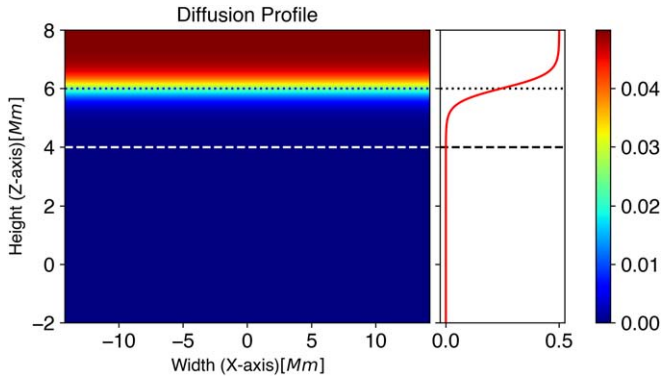

Figure 3. 2D and 1D plots of the diffusion profile. The dotted lines indicate the height at which the sigmoid is centered (z_c). The dashed lines indicate the height we consider for computing the Alfvén power spectrum.

that the sigmoid starts after 4 Mm and is centered at around 6 Mm. We use the 2D diffusion profile discussed above as a mask that multiplies the time-constant part of the diffusion coefficient (proportional to the sum of the flow speeds and the grid spacing in each Cartesian direction). The final diffusion coefficient, which is different for each equation and direction, is formed by the sum of the time-constant part and the hyperdiffusion and shock-diffusion contributions, computed as explained in Section 3.4 of M. Modestov et al. (2024). The diffusion coefficients then enter into the computations of the viscosity tensor, ohmic diffusion, and their corresponding counterparts in the energy equation, as well an an artificial term in the continuity equation that does not have a physical counterpart. For more details, the reader is referred to M. Modestov et al. (2024).

Additionally, Perfectly Matched Layer (PML) with a sponge layer is applied to the upper part of the model, from 6 Mm to 8 Mm (100 grid points), as part of the boundary conditions (M. Modestov et al. 2024). PML has proved to be an excellent wave absorber and has been employed in many previous works (E. Khomenko & M. Collados 2008; T. Felipe et al. 2010; E. Khomenko & P. S. Cally 2012; C. D. MacBride et al. 2022). As the Alfvén and sound speeds increase drastically with height in the corona, waves with large amplitudes develop in our simulation.

2.4. Broadband Driver

We employ a broadband driver designed to mimic aspects of the observed p-mode spectrum (which is shown in Figure 4). The feature of interest is the distinct peak at 3 mHz. The p-modes with frequencies much lower than this value are always evanescent in the atmosphere, so likely do not contribute to the flux of the coronal Alfvén waves. Further, given that the mode conversion process is linear, we expect a one-to-one mapping between the p-mode frequencies and those of the coronal Alfvénic waves. Hence, we also do not attempt to simulate the high-frequency regime here. To describe our driver, we use a Gaussian function centered at $P_c = 320$ s ($\nu_c \approx 3$ mHz to model the velocity amplitude in frequency space), i.e.:

$$V_n = v_0 \exp\left(-\frac{1}{2}\left(\frac{\nu_n - \nu_c}{\sigma_\nu}\right)^2\right). \tag{11}$$

Here, $v_0 = 2 \times 10^{-4}\,\mathrm{m\,s^{-1}}$ and σ_ν is the standard deviation of the Gaussian. The shape of the driver power spectrum is shown as the blue curve in Figure 4. For the driver, we consider 200 sinusoidal perturbations, with periods ($P_n = 1/f_n$) uniformly

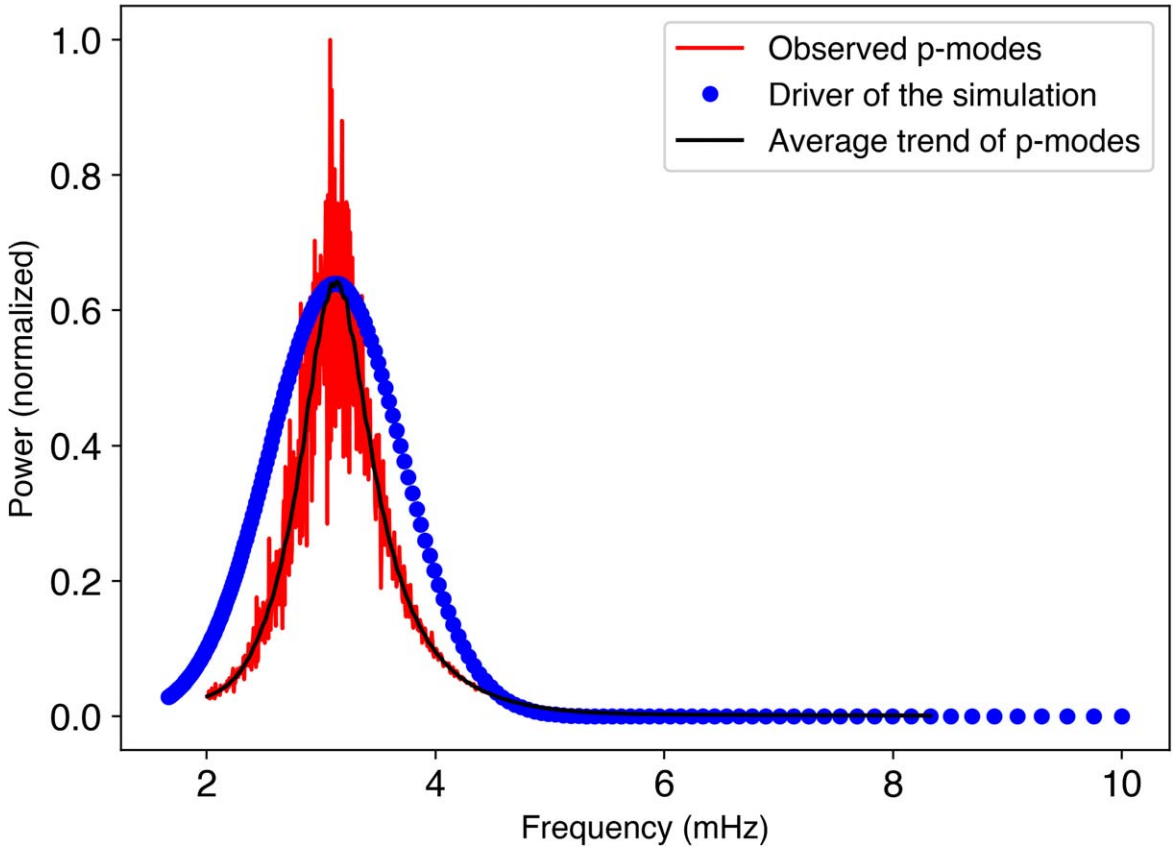

Figure 4. The frequency dependence of the wave driver, comparing the broadband driver (blue dots) used in the simulation with the observed *p*-mode power spectrum (red solid line) from Michelson Doppler Imager of the Solar and Heliospheric Observatory (E. J. J. Rhodes et al. 1997). The black line is the average trend fitted to the observed *p*-mode power spectrum.

spaced between 100 and 600 s, with the amplitude for each sinusoid given by Equation (11).

The driver is confined vertically to a few grid points close to the domain's bottom boundary ($Z = -2$ Mm, -1.25 Mm, and $X = 0$ Mm). The form of the perturbations is determined analytically as an acoustic-gravity wave (see D. Mihalas & B. Mihalas 1986; E. Khomenko & P. S. Cally 2012), ignoring the magnetic field and temperature gradient. The ratio of sound-to-Alfvén speeds squared in the driving region is $c_s^2/v_A^2 \approx 250$. Hence, we can expect the magnetic field to be dynamically unimportant and mainly acoustic modes to be excited by the driver. In accordance with D. Mihalas & B. Mihalas (1986), self-consistent perturbations of the velocity vector, pressure, and density are given by:

$$\delta V_z = \sum_{n=1}^{200} V_n \quad g(x)\exp\left(\frac{z}{2H} + k_{zi}z\right) \times \sin(\omega_n t - k_{zr}z + \Phi_n), \tag{12}$$

$$\frac{\delta p}{p_0} = \sum_{n=1}^{200} V_n |P_n| g(x)\exp\left(\frac{z}{2H} + k_{zi}z\right) \times \sin(\omega_n t - k_{zr}z + \phi_{P_n} + \Phi_n), \tag{13}$$

$$\frac{\delta \rho}{\rho_0} = \sum_{n=1}^{200} V_n |R_n| g(x)\exp\left(\frac{z}{2H} + k_{zi}z\right) \times \sin(\omega_n t - k_{zr}z + \phi_{R_n} + \Phi_n). \tag{14}$$

Here, H is the density scale height, k_{zr} and k_{zi} are real and imaginary vertical wavenumbers, and Φ_n is a random phase added to the wave at each of the 200 frequencies. The subscript "0" refers to quantities related to the unperturbed background atmosphere. The X-dependence of the pulse, denoted as $g(x)$, is defined by

$$g(x) = \exp\left(-\frac{1}{2}\left(\frac{x - x_0}{\sigma_x}\right)^2\right), \tag{15}$$

where σ_x defines the size of the pulse in the X-direction, x_0 is the location where the Gaussian is centered, and x is the horizontal coordinate. We choose $\sigma_x = 1.25$ Mm. Using a spatially localized pulse excites modes with different horizontal wavenumbers, with the mode amplitude decreasing as the absolute value of the wavenumber increases (E. Khomenko & M. Collados 2006).

The amplitudes and the relative phase shifts between the perturbations are given by

$$|P_n| = \frac{\gamma}{\omega_{i_n}}\sqrt{k_{zr}^2 + \left(k_{zi} + \frac{1}{2H}\frac{(\gamma - 2)}{\gamma}\right)^2}, \tag{16}$$

$$|R_n| = \frac{1}{\omega_{i_n}}\sqrt{k_{zr}^2 + \left(k_{zi} - \frac{1}{2H}\right)^2}, \tag{17}$$

$$|\phi_{P_n}| = \arctan\left(\frac{k_{zi}}{k_{zr}} + \frac{1}{2Hk_{zr}}\frac{(\gamma - 2)}{\gamma}\right), \tag{18}$$

$$|\phi_{R_n}| = \arctan\left(\frac{k_{zi}}{k_{zr}} - \frac{1}{2Hk_{zr}}\right). \quad (19)$$

Given the wave angular frequency, the vertical wavenumber is found from the dispersion relation for acoustic-gravity waves in an isothermal atmosphere to be

$$k_z = k_{zr} + ik_{zi} = \sqrt{(\omega_n^2 - \omega_{ac}^2)/c_s^2}, \quad (20)$$

where $\omega_{ac} = 2\pi\nu_{ac}$ is the acoustic cutoff frequency.

3. Results

Upon providing the background atmosphere and the driver, MANCHA is then used to solve the perturbations of density, pressure, magnetic field, and the velocities of the system of MHD equations (Equations (2)–(5)). Given that the mode conversions of interest are linear in nature, we keep the initial perturbations of the system small (refer to Equation (11)), to ensure the waves remain in the linear regime. We now discuss the results of the simulation in detail.

3.1. MHD Wave Projections

To differentiate the Alfvén modes from the fast and slow magnetoacoustic modes in the magnetically dominated atmosphere ($v_A > c_s$), we use the following projections onto three characteristic directions:

$$\hat{e}_{\rm long} = [\cos\phi \sin\theta,\ \sin\phi \sin\theta,\ \cos\theta], \quad (21)$$

$$\hat{e}_{\rm perp} = [-\cos\phi \sin^2\theta \sin\phi,\ 1 - \sin^2\theta \sin^2\phi, - \cos\theta \sin\theta \sin\phi], \quad (22)$$

$$\hat{e}_{\rm trans} = [-\cos\theta,\ 0,\ \cos\phi \sin\theta]. \quad (23)$$

Here, θ is the inclination of the magnetic field with respect to the vertical and ϕ is the azimuthal angle. The slow (long) projection is the radial unit vector along the magnetic field. The Alfvén (perp) projection is the asymptotic polarization direction perpendicular to the magnetic field, as suggested by P. S. Cally & M. Goossens (2008). The fast (trans) component is the cross product of the slow and Alfvén projections. These projections have been demonstrated to be rather effective in separating the perturbations related to all three modes (T. Felipe et al. 2010; E. Khomenko & P. Cally 2012). Note that below the equipartition layer ($c_s > v_A$), the longitudinal and transverse components will contain a mixture of fast and slow perturbations, as the fast mode propagates isotropically.

An example of applying the wave projections to the velocity perturbations is shown in Figure 5. For visualization, the long projection is scaled by $\sqrt{\rho_0 c_s}$ and the trans and perp projections are scaled by $\sqrt{\rho_0 v_A}$. The scalings correspond to the respective wave energy fluxes:

$$F_w = \rho \langle v^2 \rangle v_{\rm ph}. \quad (24)$$

Here, $\langle v^2 \rangle$ is the rms of the velocity amplitudes and $v_{\rm ph}$ is the phase speed. The magnitudes of the quantities in Figures 5 and 6 are then the square root of the kinetic energy flux. As the amplitude increases with height and the density drops accordingly, the scaling factor $\sqrt{\rho_0 v_{\rm ph}}$ allows for efficient visualization of the respective velocity projections along different layers, reducing the effects of wave amplification with height due to the variation in plasma parameters.

3.2. Wave Behavior

Figures 5 and 6 demonstrate that the wave behavior in the simulation is complex. However, the results for the lower solar atmosphere are comparable to the numerical results from the 3D simulations of T. Felipe et al. (2010) and E. Khomenko & P. S. Cally (2012). From Figure 6, it is clear that both the slow magnetoacoustic and Alfvén modes are able to propagate into the corona. The upward propagation of MHD waves from the lower solar atmosphere into the corona has been demonstrated in a number of previous numerical simulations, e.g., slow modes (V. H. Hansteen et al. 2002; G. J. J. Botha et al. 2011) and Alfvén modes (E. Khomenko & P. S. Cally 2019). In contrast, there is little signature of the fast-mode energy present. This is because the fast mode suffers significant reflection in a region above the equipartition layer, which is clearly observed in the middle panel of Figure 5. Above this region, the modes are evanescent in the corona (e.g., J. V. Hollweg 1978; B. Leroy & S. J. Schwartz 1982; S. J. Schwartz & B. Leroy 1982).

3.2.1. Acoustic Modes

Throughout the atmosphere, the acoustic modes are subject to reflections. For slow magnetoacoustic waves in a strongly magnetized environment ($c_s < v_A$), there are then two sources of wave reflection present: the gravitational stratification and also from regions with significant gradients in the pressure scale height (e.g., B. Roberts 2006; G. J. J. Botha et al. 2011). Figure 7 displays the cutoff frequency arising from gravitational stratification (given by Equation (1)), and it varies across the domain, peaking at ~4.5 mHz. In the current model, slow waves with frequencies less than ~4 mHz should be reflected before they reach the equipartition layer.

Figure 5 shows a number of locations where there is substantial wave reflection due to strong gradients in the pressure scale height (H_p), see Figures 1 and 2 for the sound-speed profiles. These are visible as the horizontal stripes across the domain, notably at a height of ~2 Mm in the slow projection. We expect this boundary to form a resonance cavity in the lower atmosphere, with the potential for standing modes to exist (e.g., Y. D. Zhugzhda 2007, 2008; G. J. J. Botha et al. 2011; T. Felipe et al. 2020). Another horizontal stripe at 6 Mm marks where the PML boundary conditions start and the diffusion profile reaches a value half its maximum (see Figure 3). This combination of factors leads to an artificial reflection point. Above 6 Mm, the waves are damped rapidly, showing the effectiveness of the combined PML and artificial diffusion.

It is insightful to examine how the waves evolve with time in the system. Figure 6 shows the velocity projections for a single column of the simulation (its location in the domain is at $X = 4.55$ Mm, marked by the vertical dashed lines in Figure 5). For this column, the magnetic field inclination has values $(\theta, \phi) = (30^\circ, 56^\circ)$ at the equipartition layer. It can be seen that the excited fast acoustic waves propagate upward and are either split into slow magnetoacoustic waves or mode-converted to fast magnetoacoustic waves at the equipartition layer (indicated by the solid line running across all six panels). In the left panels of Figure 6, the propagating slow waves above the equipartition layer experience strong reflection from the locations with steep temperature gradients of the transition region. This feature was not seen in the simulations of E. Khomenko & P. S. Cally

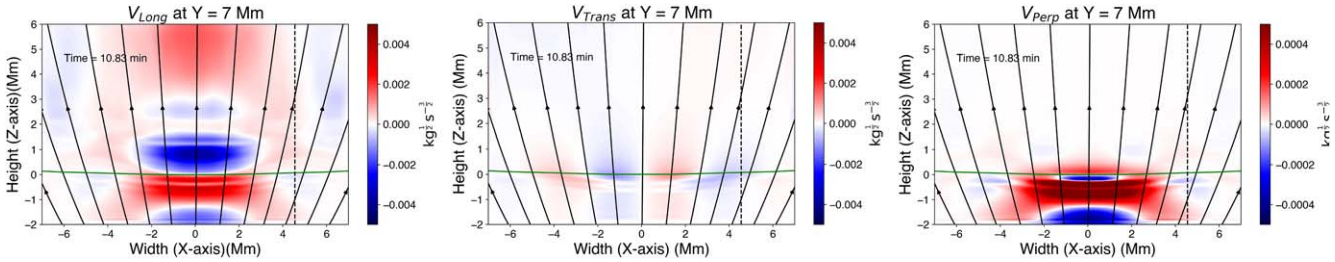

Figure 5. Velocity projections of slow (left), fast (middle), and Alfvén (right) waves at a snapshot at 1163 s. The green contour is the equipartition layer. The vertical dashed line is where $\theta = 30^{\circ}$ and $\phi = 56^{\circ}$ at the equipartition layer. The velocities are scaled by a factor of $\sqrt{\rho_0 c_s}$ for the left panel and $\sqrt{\rho_0 v_A}$ for the middle and right panels.

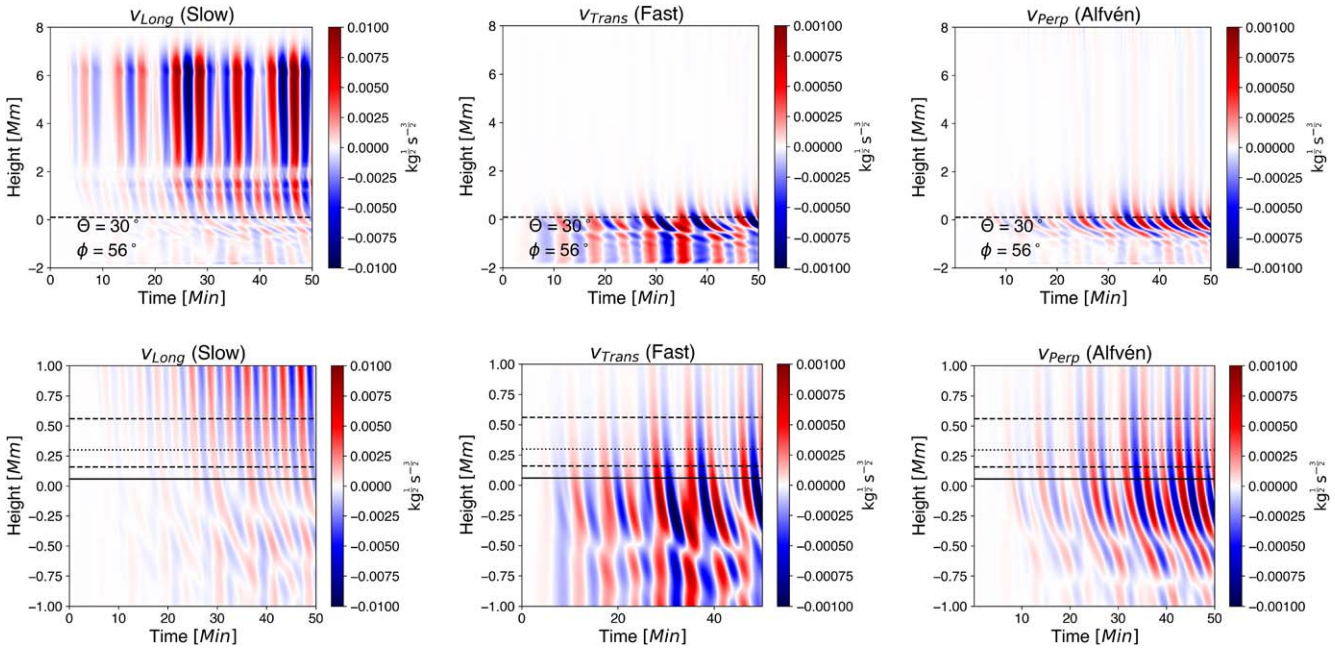

Figure 6. Time evolutions of velocity projections of slow (left), fast (middle), and Alfvén (right) waves for a column of the simulation. The location in the domain is shown by the vertical line in Figure 5. The inclination angle and the azimuthal angles are $(\theta, \phi) = (30^{\circ}, 56^{\circ})$ at the equipartition layer. The plots in the second row are similar but zoomed in to a vertical range of −1 Mm to 1 Mm for better clarity. The solid line is the equipartition layer and the region between the two dashed lines corresponds to the fast wave reflection region. The dotted line is the fast wave reflection region, which is estimated by taking the period $P_n = P_c$. All the velocity projections are scaled by a factor of $\sqrt{\rho_0 c_s}$ for the left panel and $\sqrt{\rho_0 v_A}$ for the middle and right panels.

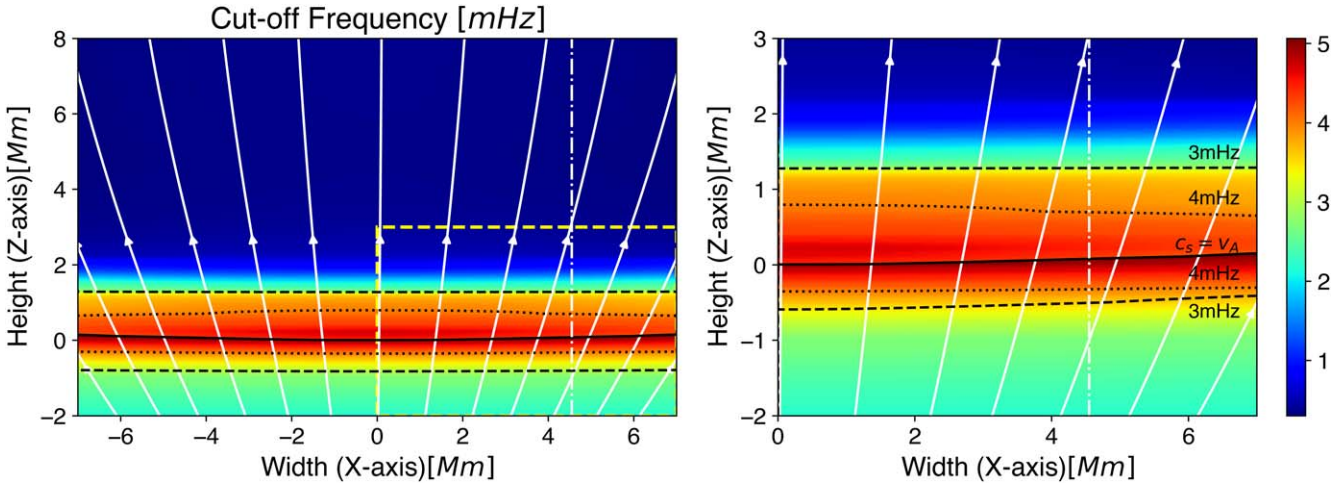

Figure 7. Cutoff frequency across the background condition. The white contours refer to the magnetic field lines. The vertical white dashed–dotted line refers to the slit we considered to achieve the results in Figure 6. The solid black line across the domain is the equipartition layer ($c_s = v_A$). The dashed and dotted lines refer to the cutoff layers where $\nu_{ac} = 4$ mHz and 3 mHz, respectively. We have clipped the regions within the yellow dashed rectangular box to achieve the plot on right for better visualization purposes.

(2012), but is similar to the 2D simulations of I. Santamaria et al. (2015). The returning slow magnetoacoustic modes should then also be able to mode convert or be transmitted as they pass back through the equipartition layer.

The upwardly traveling slow waves then propagate quickly through the coronal part of the simulation, due to the increased sound speed. The slow waves suffer reflection around 6 Mm, due the onset of the diffusion profile and PML layers. This leads to the variable flux of downward-propagating slow modes, indicated by the varying slopes in the time–distance diagram of the longitudinal velocity component.

3.2.2. Transverse Modes

In the middle panels of Figures 5 and 6, the fast magnetoacoustic wave is chosen by the orthogonal projection $\hat{e}_{\rm trans}$ above the equipartition layer, but it is a mixture of wave modes below the equipartition layer. The enhancement of the transverse component about the equipartition is dominated by downward-propagating, reflected modes (middle panels of Figure 6). The reflection of fast magnetoacoustic waves back into the lower atmosphere occurs up to around 2 Mm above the equipartition layer. The region of wave reflection will differ for modes with different ω and k_h. In Figure 6, we indicate the reflection region for a wave with $k_h = 1.07$ Mm^{-1} (equivalent to the full-width half-maximum of the driver pulse). The lower dashed line refers to the height where $\omega = 2\pi/P_n$, for $P_n = 100$ s, and the upper dashed line refers to the region where $P_n = 600$ s. The dotted line refers to the region where $P_n = P_c$, i.e., 320 s, where the driver is centered. As the fast-to-fast conversion is linear, the fast magnetoacoustic modes generated in this simulation should be reflected strongly below 1 Mm. This is clearly seen in the time–distance plots. The observed pattern of reflection is comparable to that observed in previous simulations (e.g., T. Felipe et al. 2010; E. Khomenko & P. S. Cally 2012). As mentioned, very little fast magnetoacoustic (or transverse) energy is able to reach the corona.

Due to the presence of multiple wave frequencies and the reflection of slow and Alfvén waves from the transition region, the pattern below ~ -1 m is more complicated than in previous simulations. This is because the mode conversion is possible between all modes in this region (P. S. Cally 2022). Although interesting, we do not attempt to disentangle the relationships between the reflected waves.

3.2.3. Alfvén Modes

The Alfvén waves are separated by the projection $\hat{e}_{\rm perp}$ from Equation (22). Given the strong reflection of the transverse wave modes observed within Figure 6, it can be expected that some of the fast-wave energy is converted to upwardly propagating Alfvén waves, hence the occurrence of the perpendicular component in the corona (e.g., as also found in the simulations of T. Felipe et al. 2010; E. Khomenko & P. S. Cally 2012). The Alfvén waves are reflected throughout the simulation, due to gradients in the Alfvén speed (e.g., J. V. Hollweg & V. J. Hollweg 1978; S. J. Schwartz et al. 1984), and some of the wave energy is reflected back toward the photosphere. The steepest gradients in the Alfvén speed occur at the transition region (see Figures 1 and 2). The reflected Alfvén waves leave a significant signature of downward propagation in the right panels of Figure 6. This reflection reduces the amount of Alfvén wave energy able to reach the upper part of the simulation (compared to the results of E. Khomenko & P. S. Cally 2012).

Hence, irrespective of the wave types, the transition region acts as a partial barrier to all the upward-propagating waves within this simulation. It has been shown that transverse structuring can aid the transmission of waves to the corona (E. Khomenko & P. S. Cally 2019; S. J. Skirvin & T. Van Doorsselaere 2024), although there is a suggestion that the rate of expansion of the magnetic field in the lower atmosphere is the dominant influence on the wave energy flux through the transition region (at least for Alfvén waves; Y. Taroyan & T. Borradaile 2024). Here, the sunspot is best described as a thick flux tube model that rapidly expands in the lower atmosphere, which leads to strong reflection.

3.3. Coronal Power Spectra

To determine the coronal power spectra of different wave modes, we take the Fourier transform of the individual time series at each grid point for each velocity projection. The time series used are taken across the sunspot domain at the height of $Z = 4$ Mm. The squared absolute value of the Fourier coefficients is taken and averaged across all time series, to obtain the average power spectra across the sunspot. The averaging across the sunspot will somewhat mimic line-of-sight integration through the corona at the limb, incorporating the wave behavior across magnetic fields with various inclination angles.

Figure 8 shows the coronal power spectra of fast, slow, and Alfvén waves. In addition to these curves, we also show the power spectrum of the velocity projection v_z, averaged across the width of the driving pulse (σ_x) at the height of $Z = -1.65$ Mm. It can be seen that the coronal power spectra for all the wave modes have an enhanced power that is clearly located at a different frequency from that of the driver (with a dominant driving frequency at $\approx$3 mHz). Fitting a Gaussian function to the power enhancement for the Alfvén waves reveals that the peak occurs at a frequency of ~4 mHz. The frequency is comparable to that estimated from the coronal Doppler velocity fluctuations associated with Alfvénic waves (R. Morton et al. 2019). We note that the high-frequency peaks in the coronal power spectra between 10 and 50 mHz are caused by the spurious excitation of waves due to the reflection from the periodic boundaries.

As discussed in the introduction, this phenomenon arises due to the frequency filtering effects present for magnetoacoustic wave propagation. The upward-propagating acoustic modes are subject to frequency-dependent reflection below the equipartition layer, leading to filtering. The characteristics of the acoustic wave power spectra are then passed on to the other wave modes during the linear mode conversion processes. This is indicated by the fact that all the coronal power spectra display an enhancement of power in the same frequency range (and have similarly shaped power spectra).

For the current simulation, the coronal slow modes have substantially greater power than the coronal Alfvén modes—although, as discussed, there is a nonphysical reflection of the coronal slow waves due to the numerical implementation, which means the magnitude of the power difference between the slow and Alfvén modes is likely inflated. The transverse waves have a factor of ~10^5 less power than the Alfvén waves, which is expected due to the near total reflection of the fast modes.

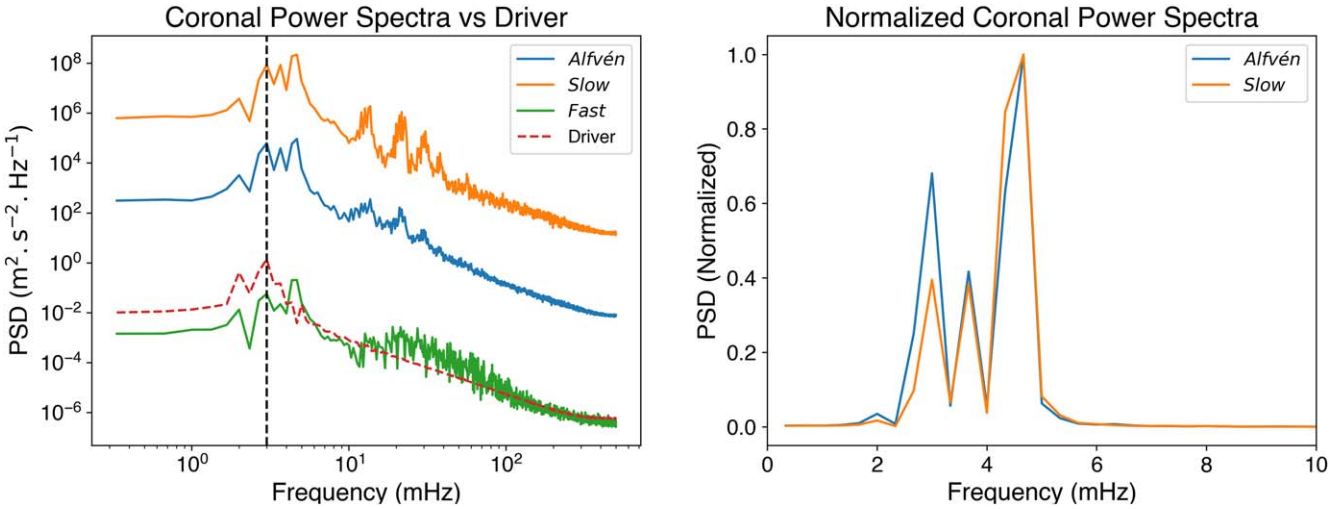

Figure 8. Coronal power spectra for the MHD wave modes. The figure on the left shows the average power spectra for the slow, Alfvén, and fast velocity projections, indicated by the orange, blue, and green curves, respectively. For all modes, the coronal Alfvén power spectrum peaks around 4.5 mHz, with the frequency indicated by the vertical black dotted line. The red dashed curve is the averaged power spectrum of the velocity projection v_z at the location of the driver. The peak frequency of the driver is shown by the vertical black dashed line. The figure on the right shows the normalized average power spectra for slow and Alfvén projections.

4. Conclusion and Discussion

It is well established that the coronal Alfvénic power spectrum has an enhancement around 4 mHz (S. Tomczyk et al. 2007; R. Morton et al. 2019), and the underlying cause behind the enhanced power at this frequency range has been the subject of debate. Previous work has suggested that *p*-modes (which have a peak power of around 3 mHz) could be responsible, mode converting first to fast magnetic waves and then to Alfvén waves (e.g., P. S. Cally & S. C. Hansen 2011; S. C. Hansen & P. S. Cally 2012; E. Khomenko & P. S. Cally 2012; P. S. Cally 2017). Here, we demonstrate by direct numerical simulation that the enhancement of the coronal Alfvénic power spectrum can be directly connected to the internal acoustic oscillations.

As discussed in the introduction, the temperature structure of the lower solar atmosphere is a natural filter for the upward-propagating acoustic waves, truncating the power spectra for low frequencies ($\nu < \nu_{ac}$). The subsequent mode conversions—i.e., fast to fast and fast to Alfvén—are linear, so the filtered power spectrum of the *p*-modes is imparted on the resultant transformed wave modes. This is clearly seen in the simulations when measuring the coronal power spectrum for all wave modes. The peak of the coronal power spectrum will depend upon the location of the equipartition layer with respect to the temperature minimum (where the highest-value frequency cutoff occurs). In the current model, the equipartition layer is close to, but below, the temperature minimum, hence the upwardly propagating waves are subject to nearly the maximal filtering. Should the equipartition layer be lower, then the filtering of the *p*-mode spectrum would be less and the Alfvénic power spectrum would likely peak at a lower frequency.

The slow magnetoacoustic modes continue to feel the effect of the cutoff above the equipartition layer and should be more strongly filtered. This is seen when comparing the normalized coronal power spectrum for the slow and Alfvén waves (the right panel of Figure 8), where the slow waves have less power at lower frequencies. The magnetic field inclination (θ) will also play a role in shaping the coronal wave power spectrum, as it further modifies the cutoff frequency. This will essentially only affect the slow modes, though.

We note that in the current simulation, there is a limited range of magnetic field inclination angles ($30^\circ < \theta < 40^\circ$). The range of angles is particularly suited to the fast-to-Alfvén conversion. Further simulations are required that incorporate a broader selection of magnetic field inclinations (both θ and ϕ) to see whether the peak from the average coronal power spectrum still occurs at 4 mHz. We speculate that this will be the case, as the coronal Alfvén spectrum is shaped by the filtering of the fast acoustic modes below the equipartition layer, which is largely independent of inclination.

The results from the sunspot should also be representative of wave dynamics in network fields in the quiet Sun. The foreseeable differences are the relative heights of the equipartition layer and the temperature minimum. In network elements, the equipartition layer is likely to occur above the temperature minimum (e.g., see the atmospheric structure of network elements in E. Khomenko et al. 2008), although this will depend upon the magnetic field strength. This might introduce additional filtering of the fast acoustic modes before they are converted to fast magnetoacoustic modes. However, the minimum plasma temperature in the network elements is likely greater than that in the sunspots (it could potentially be up to 1000 K more, based on 1D semi-empirical models of sunspots and network elements). This means the frequency filtering could be less severe and may not extend to frequencies of 5 mHz. Further simulations would be required to confirm this.

It is worth highlighting that we derive an averaged coronal Alfvén power spectrum at 4 Mm above the photosphere, far below the heights at which CoMP has previously made measurements. We believe that the spectrum would remain largely unchanged as the waves propagate higher in the corona. These Alfvén waves are subject to amplification with height, due to the drop in density with height, and observations suggest they remain linear. Furthermore, observations indicate there is weak Alfvénic wave damping in the quiet Sun (A. K. Tiwari et al. 2021) and coronal holes (R. J. Morton et al. 2015) from frequency-dependent mechanisms, such as resonant absorption

and phase mixing. Hence, we expect the overall shape of the power spectrum to remain largely unchanged.

Acknowledgments

H.M. thanks Northumbria University for financial support. R.J.M. would like to thank the UKRI for financial support via a UKRI Future Leader Fellowship (RiPSAW MR/T019891/1). E.K. is grateful for the support from the Spanish Ministry of Science and Innovation through the grant PID2021-127487NB-I00. The authors would like to thank K. Karampelas, T. Duckenfield, and R. Sharma for reading drafts and valuable discussions. The data that support the findings of this study are available from the corresponding author upon reasonable request.

ORCID iDs

Hemanthi Miriyala https://orcid.org/0000-0002-2235-3216
Richard J. Morton https://orcid.org/0000-0001-5678-9002
Elena Khomenko https://orcid.org/0000-0003-3812-620X
Patrick Antolin https://orcid.org/0000-0003-1529-4681
Gert J.J. Botha https://orcid.org/0000-0002-5915-697X

References

Bogdan, T. J., & Judge, P. G. 2006, RSPTA, 364, 313
Botha, G. J. J., Arber, T. D., Nakariakov, V. M., & Zhugzhda, Y. D. 2011, ApJ, 728, 84
Cally, P. S. 2006, RSPTA, 364, 333
Cally, P. S. 2017, MNRAS, 466, 413
Cally, P. S. 2022, MNRAS, 510, 1093
Cally, P. S., & Bogdan, T. J. 1997, ApJ, 486, L67
Cally, P. S., & Goossens, M. 2008, SoPh, 251, 251
Cally, P. S., & Hansen, S. C. 2011, ApJ, 738, 119
Centeno, R., Collados, M., & Trujillo Bueno, J. 2006, ApJ, 640, 1153
Cranmer, S. R., & van Ballegooijen, A. A. 2005, ApJS, 156, 265
Edwin, P. M., & Roberts, B. 1983, SoPh, 88, 179
Felipe, T. 2012, ApJ, 758, 96
Felipe, T., Khomenko, E., & Collados, M. 2010, AJ, 719, 357
Felipe, T., Kuckein, C., González Manrique, S. J., Milic, I., & Sangeetha, C. R. 2020, ApJL, 900, L29
Fontenla, J. M., Avrett, E. H., Loeser, R., et al. 1993, ApJ, 406, 319
Gao, Y., Guo, M., Van Doorsselaere, T., Tian, H., & Skirvin, S. J. 2023, ApJ, 955, 73
Goossens, M., Terradas, J., Andries, J., Arregui, I., & Ballester, J. L. 2009, A&A, 503, 213
Goossens, M. L., Arregui, I., & Van Doorsselaere, T. 2019, FrASS, 6, 20
Hansen, S. C., & Cally, P. S. 2012, ApJ, 751, 31
Hansteen, V. H., Wikstøl, Ø., Brynildsen, N., et al. 2002, in IAU Coll. 188, SOLMAG 2002, ed. H. Sawaya-Lacoste (Noordwijk: ESA Publications), 183
Hollweg, J. V. 1978, GeoRL, 5, 731
Hollweg, J. V., & Hollweg, V. J. 1978, SoPh, 56, 305
Jess, D., Reznikova, V., Van Doorsselaere, T., Keys, P., & Mackay, D. 2013, ApJ, 779, 168
Jess, D. B., Morton, R. J., Verth, G., et al. 2015, SSRv, 190, 103
Jess, D. B., & Verth, G. 2016, GMS, 216, 449
Jiménez, A., Garcìa, R. A., & Pallé, P. L. 2011, ApJ, 743, 99
Khomenko, E., & Cally, P. 2012, ApJ, 746, 68
Khomenko, E., & Cally, P. S. 2012, ApJ, 746, 68
Khomenko, E., & Cally, P. S. 2019, ApJ, 883, 179
Khomenko, E., & Collados, M. 2006, ApJ, 653, 739
Khomenko, E., & Collados, M. 2008, ApJ, 689, 1379
Khomenko, E., Collados, M., & Felipe, T. 2008, SoPh, 251, 589
Kuniyoshi, H., Shoda, M., Morton, R. J., & Yokoyama, T. 2024, ApJ, 960, 118
Landgraf, V. 1997, AN, 318, 129
Leroy, B., & Schwartz, S. J. 1982, A&A, 112, 84
Low, B. 1980, SoPh, 67, 57
MacBride, C. D., Jess, D. B., Khomenko, E., & Grant, S. D. T. 2022, ApJ, 938, 154
Mihalas, D., & Mihalas, B. 1986, PhT, 39, 90
Modestov, M., Khomenko, E., Vitas, N., et al. 2024, SoPh, 299, 23
Morton, R., Weberg, M., & McLaughlin, J. 2019, NatAs, 3, 223
Morton, R. J., Mooroogen, K., & Henriques, V. M. J. 2021, RSPTA, 379, 20200183
Morton, R. J., Sharma, R., Tajfirouze, E., & Miriyala, H. 2023, RvMPP, 7, 17
Morton, R. J., Tomczyk, S., & Pinto, R. 2015, NatCo, 6, 7813
Nakariakov, V. M., & Kolotkov, D. Y. 2020, ARA&A, 58, 441
Osterbrock, D. E. 1961, ApJ, 134, 347
Pizzo, V. J. 1986, ApJ, 302, 785
Rhodes, E. J. J., Kosovichev, A. G., Schou, J., Scherrer, P. H., & Reiter, J. 1997, SoPh, 175, 287
Roberts, B. 2006, RSPTA, 364, 447
Sakurai, T. 2017, PJAB, 93, 87
Santamaria, I., Khomenko, E., & Collados, M. 2015, A&A, 577, A70
Schunker, H., & Cally, P. S. 2006, MNRAS, 372, 551
Schwartz, S. J., Cally, P. S., & Bel, N. 1984, SoPh, 92, 81
Schwartz, S. J., & Leroy, B. 1982, A&A, 112, 93
Skirvin, S. J., Gao, Y., & Van Doorsselaere, T. 2023, ApJ, 949, 38
Skirvin, S. J., & Van Doorsselaere, T. 2024, A&A, 683, A61
Spruit, H. C. 1982, SoPh, 75, 3
Spruit, H. C., Bogdan, T. J., Spruit, H. C., & Bogdan, T. J. 1992, ApJL, 391, L109
Taroyan, Y., & Borradaile, T. 2024, A&A, 691, A55
Tiwari, A. K., Morton, R. J., & McLaughlin, J. A. 2021, ApJ, 919, 74
Tomczyk, S., McIntosh, S. W., Keil, S. L., et al. 2007, AGUFM, 2007, SH21A–0289
Van Doorsselaere, T., Srivastava, A. K., Antolin, P., et al. 2020, SSRv, 216, 140
Vögler, A., Shelyag, S., Schssler, M., et al. 2005, A&A, 429, 335
Zhugzhda, Y. D. 2007, AstL, 33, 622
Zhugzhda, Y. D. 2008, SoPh, 251, 501